AIChE

A Depth Filtration Model of Straining Within the Void Networks of Stainless Steel Filters

John C. Price and Graham Peter Matthews
School of Geography, Earth and Environmental Sciences, University of Plymouth, Devon PL4 8AA, U.K.

Kevin Quinlan and John Sexton
Porvair Filtration Group Ltd, Fareham PO15 5RT, U.K.

Alexander G. de G. Matthews
St. John's College, Cambridge CB2 1TP, U.K.

DOI 10.1002/aic.11925

A depth filtration model has been developed, based on the three-dimensional void network model Pore-Cor. The geometry of the void network is fitted, by means of an eight-dimensional Boltzmann annealed amoeboid simplex, to the porosity and percolation characteristics of stainless steel sintered filters measured by mercury porosimetry. Preferential and critical flow paths through the network are calculated. Particles from an experimental size distribution are fed along these flow-biased paths, and when straining occurs, the flow paths are re-calculated. We show that the model usefully reproduces experimental filtration efficiencies as a function of pressure drop, measured by single pass tests. We also offer a critique of current measurements of filtration efficiency, suggesting the use of a new "alpha efficiency" rather than the standard beta efficiency. The model is currently being adapted to accept porometry as well as porosimetry data, hence avoiding the use of mercury. © 2009 American Institute of Chemical Engineers *AIChE J,* 55: 3134–3144, 2009
Keywords: filter, stainless steel, void network model, straining, capture efficiency

Introduction

Before release to the market place, new filtration products require time-consuming and expensive "wet bench" testing and validation to ensure they perform to specified standards and customer requirements. There is, therefore, an incentive to adapt a theoretical network model so that it forms a predictive tool sufficiently reliable that it will reduce the need for wet bench procedures.[1]

Depth filtration or filter medium filtration is a common process used to remove solid particulate matter from dilute liquid suspensions by means of a series of capture mechanisms, of low to intermediate efficiency, within the void structure of a porous medium (the filter).[2–4] Network models, as introduced by Fatt[5] and others, are well suited to the study of the behavior of particles and fluid within a filter medium.[6] The void networks within the porous medium are represented by a network of interconnected bonds or arcs meeting together at nodes. The network, which is often two-dimensional,[7] is arranged with a prescribed or random geometry that has an estimated or measured connectivity. The lengths of the arcs can either be random or related to their diameters, for example directly or inversely proportional to them. The arc diameters can be randomly chosen from void size distributions obtained from experimental techniques such as mercury porosimetry or photo-micrographic techniques.[8] Different stochastic realizations may be generated and presented as averages of the media.[9] Typical of the approach

---

Correspondence concerning this article should be addressed to G. P. Matthews pmatthews@plymouth.ac.uk

Table 1. Experimental and Simulated Sample Characteristics

Sample	Size for 98% Removal Efficiency (μm)	Maximum Effective Pore Size for Particle Removal (μm)	Experimental Absolute Liquid Permeability (m^2)
S16	3.2	13	1.80×10^{-14}
S21	5.9	23	8.01×10^{-14}
S26	12	34	1.60×10^{-13}
S36	26	67	4.61×10^{-13}
S41	40	94	8.96×10^{-13}

is the work of Sahimi and coworkers,[10–12] who have developed generalized models of fines migration through regular 3D and 2D void networks, with void sizes set mathematically rather than directly from experiment. The models take into account the particles trajectories as well as straining, and are compared with the results of experiments carried out on a sandpack. Other studies, which range from phenomenological and semi-empirical[13] to totally mathematical, have been reviewed by Sahimi et al.[14] and Elmelech.[15]

We present an approach which builds on this previous work. As proposed and trialed by Sexton,[16] it uses a three-dimensional void network that removes the excessive effects of single straining events which occur in two-dimensional models.[17] The sizes of the void features and the overall network geometry are adjusted, by means of an eight-dimensional Boltzmann-annealed amoeboid simplex, to match the percolation characteristics of an experimental filter determined by mercury porosimetry. The flow capacity of each arc of the network is then calculated using parameterized Navier Stokes equations. The overall flow capacity of the network is calculated with an operational research network capacity algorithm[18] applied to the entire network and its periodic boundary replicates.[19] The algorithm calculates the maximum flow which can be fed through the void network, while minimizing "cost," i.e., the additional swirling of fluid through routes which do not contribute additionally to the flow capacity. Critical flow routes are identified by interrogating the algorithm. Particles chosen from experimental or pseudo-experimental size distributions are then fed singly, rather than in batches,[10] along the critical flow routes. If straining occurs then a feature of the filter is blocked, and the critical flow routes re-calculated. At each straining event, the filter efficiency of the filter for each particle size is measured, and also the reduction in absolute liquid permeability of the filter and the resulting pressure drop across the filter. We compare the simulation to "single pass" wet bench tests, and to the estimates of filtration efficiency and maximum pore size based on porometry measurements.

Experimental

Samples

To test the modeling, samples were needed which were highly homogenous, robust, and reproducible. Therefore, we chose to use Porvair "Sinterflo" filters made by the sintering of stainless steel powder. The filters for the wet bench tests were in the form of discs of gross diameter 140 mm, and active diameter exposed to the suspension of 120 mm. The filters were of thickness 3 ± 0.15 mm, and covered a range of five commercial grades. The sizes for 98% efficiency and the maximum effective pore sizes for particle removal, Table 1, are those quoted commercially, based on wet bench testing and porometry. For mercury porosimetry, the samples were 14 mm diameter and 3 ± 0.15 mm thick.

Apparatus and methods

Mercury porosimetry was carried out using a Micromeritics Autopore III instrument. The data was corrected for the compressibility of the samples using Pore-Comp software.[20]

Porometry was performed using a prototype instrument constructed by Porvair Filtration Group (PFG), identical in operation to previous Coulter porometers. A patent liquid known as "Porofil" was placed on top of the filter to be measured. The chamber above the liquid was filled with nitrogen, and its pressure increased. This caused the fluid to be forced down onto the surface of the filter. As soon as the nitrogen pressure was greater than or equal to the least capillary pressure within the filter, the liquid broke through the filter, followed by nitrogen, and a nitrogen flow rate was detected. The increasing nitrogen flow rate was then measured with increasing pressure. The particle capture efficiency and maximum pore size was then estimated from the difference between the pressure vs. flow-rate characteristics with and without the Porofil fluid.

Direct measurements of filter efficiency were carried out using a pass test rig constructed by PFG, using a single pass protocol[4] (Figure 1). The test fluid was DTD585 aviation grade hydraulic oil, equivalent to Castrol Aero HF 585B. The rig was first run empty, i.e., with no test filter and no contaminant. The oil was then pumped through it at 8.3×10^{-5} m^3/s (5 l/min) or 1.2×10^{-4} m^3/s (7 l/min), the flow rates having been chosen on the basis of preliminary tests described later.

For purposes of description and discussion, we will define four spherical-equivalent sizes only, s_1, s_2, s_3, s_4 ($s_1 < s_2 < s_3 < s_4$), although in practice, between 6 and 10 sizes were used, s_1, s_2, …, $s_{\max}$. For the experimental tests, s represented the maximum of the corresponding size interval, so for the four sizes used in the discussion, the intervals which we will refer to as s_1, s_2, s_3, and s_4 were in fact 0 to s_1, s_1 to s_2, s_2 to s_3, and s_3 to s_4, respectively. The numbers of particles upstream, N_{u1} (background), N_{u2} (background), N_{u3} (background), N_{u4} (background) at these sizes, and the

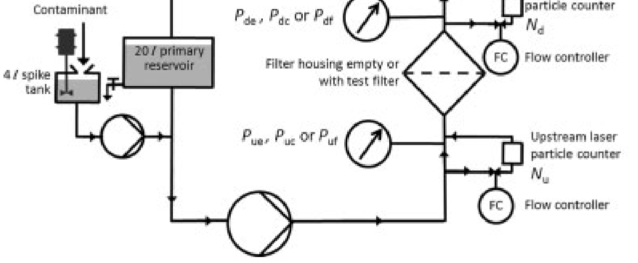

Figure 1. Schematic diagram of a single pass test apparatus.

equivalent measurements downstream, N_{d1} (background), N_{d2} (background), N_{d3} (background), N_{d4} (background), were measured with a Hiac Royco particle counter incorporating a Beta Ratiometer This device comprised two laser particle size counters, and manually operated flow rate controllers to balance the flow rate through each counter loop, as shown in Figure 1. Pumping continued until all the background particle counts reached a low and constant value, indicating that the clean-up filter could not clean the oil further from contamination from previous runs. The upstream and downstream pressures P_{ue} and P_{de} were then measured to give the "housing loss" ΔP_h, defined as ($P_{ue} - P_{de}$).

Then a test filter was inserted into the housing. Oil was pumped at 8.3×10^5 m^3/s or 1.2×10^4 m^3/s around the main circuit. The "clean" pressure losses were measured upstream, P_{uc}, and downstream P_{dc}; 4×10^{-3} m^3 (4 l) of oil was then tapped from the primary reservoir. One gram of Accublast glass beads as contaminant was added to this oil, and the suspension was poured into the spike tank where it was stirred. For a main circuit pumping rate of 1.2×10^{-4} m^3/s, the suspension was then pumped into the main flow at a rate of 8.3×10^{-7} m^3/s (50 ml/min), corresponding to a contaminant dosage rate of 2.1×10^{-3} g/s (12.5 mg/min). For a main circuit pumping rate of 8.3×10^{-5} m^3/s, the suspension was pumped in at a proportionally reduced rate of 6.0×10^{-7} m^3/s (36 ml/min). The upstream and downstream pressures P_{uf} and P_{df} were then measured, together with the upstream and downstream particle sizes and numbers, N_{u1}, N_{u2}, … and N_{d1}, N_{d2}, ….

Standard Characterization of Filters

The most direct measure of filter efficiency is to compare the capture efficiency C at any particular particle size s, for example at size 2:

$$C_{s2} = 1 - \frac{\text{Number of particles of size } s_2 \text{ downstream}}{\text{Number of particles of size } s_2 \text{ upstream}} = \frac{N_{u2} - N_{d2}}{N_{u2}} \quad (1)$$

The cumulative capture efficiency C_{cum} is defined as the sum of all efficiencies of capture up to and including that size, for example at size 2:

$$C_{cum2} = 1 - \frac{N_{d1} + N_{d2}}{N_{u1} + N_{u2}} \quad (2)$$

We also define a normalized cumulative efficiency $\mathcal{C}_{cum}$. If C_{cum} tends to $C_{cum,max}$ as s tends to s_{max}, then the normalized cumulative efficiency is:

$$\mathcal{C}_{cum} = \frac{C_{cum}}{C_{cum,max}} \quad (3)$$

Filters can be characterized in terms of a beta ratio β, which ranges from 1 (no filtration) to infinity (total filtration). It is defined as number of particles greater than the specified size upstream of the filter, divided by the equivalent number downstream.

The defining equation, for size s_1, is:

$$\beta_{s1} = \frac{\text{Number of particles} > \text{size } s_1 \text{ upstream}}{\text{Number of particles} > \text{size } s_1 \text{ downstream}} = \frac{N_{u2} + N_{u3} + N_{u4}}{N_{d2} + N_{d3} + N_{d4}} \quad (4)$$

For modeling purposes and also frequently in experimental measurements, individual particle sizes s_1, s_2, … are used which are considerably different from each other, so it is most representative to define the beta ratio β' as referring to size range above and including the specified size, i.e., for size s_1:

$$\beta'_{s1} = \frac{\text{Number of particles} \geq \text{size } s_1 \text{ upstream}}{\text{Number of particles} \geq \text{size } s_1 \text{ downstream}} = \frac{N_{u1} + N_{u2} + N_{u3} + N_{u4}}{N_{d1} + N_{d2} + N_{d3} + N_{d4}} \quad (5)$$

The filter efficiency rating E is calculated from the β ratio for each value of s, using the following relationship which is incorrect in a standard text[4] and often misquoted:

$$E_s = \frac{\beta_s - 1}{\beta_s} \quad (6)$$

The corresponding parameter E', which includes the stated size, obeys an analagous relationship to β' rather than β.

The normalized relative pressure drop $\Delta\mathcal{P}_{rel}$ is defined as:

$$\Delta\mathcal{P}_{rel} = \frac{\text{Current pressure drop} - \text{housing loss}}{\text{Clean pressure drop} - \text{housing loss}} = \frac{\Delta P_f - \Delta P_h}{\Delta P_c - \Delta P_h} = \frac{P_{uf} - P_{df} - P_{ue} + P_{de}}{P_{uc} - P_{dc} - P_{ue} + P_{de}} \quad (7)$$

The blockage B of the filter may be also be calculated, defined as:

$$B = 1/\Delta\mathcal{P}_{rel} \quad (8)$$

When modeling, there is no housing loss, and therefore B is defined simply as

$$B_{model} = \frac{\text{Clean pressure drop}}{\text{Working pressure drop}} = \frac{\text{Absolute permeability of working filter}}{\text{Absolute permeability of clean filter}} = \frac{k_f}{k_c} \quad (9)$$

The method of calculating the absolute permeabilities k is described below.

For practical purposes, C, $\mathcal{C}$, B, and E above are usually multiplied by 100% and expressed as percentages.

Problems with the characterization of filters

The characterization of filters is fraught with both theoretical and experimental difficulties, which will be briefly discussed in the context of the present work. For purposes of discussion, we will assume that s_1 represents "fines," i.e., particles that remain in the main body of the test liquid, even after the use of so-called "clean-up filters," because they are too fine to be removed; they thus represent a "background" particle size. s_2 and s_3 represent particles capable of being filtered within the body of the filter. In practice, these higher size ranges also contain particles which effectively act as fines, but we will ignore those, so that N_{u2} (background), N_{u3} (background), … are zero, and N_{d2} (background), N_{d3} (background), … are also zero. s_4 is a size of particle which forms a filter cake at the filter surface.

Suppose we study a filter using a single pass test for which the oil contains a large number fraction of fines from previous tests. Then

$$N_{u1}(\text{background}) = N_{d1}(\text{background}) = N_{u1} = N_{d1} \gg N_{u2}, N_{d2}, N_{u3} \ldots \qquad (10)$$

Under these conditions, Eq. 4 shows that β_{s1} gives a falsely high impression of the filter performance at size s_1, because the large values of N_{u1} and N_{d1} are missing from the definition. Conversely, it follows from Eq. 5 that if N_{u1} and N_{d1} are large then $\beta'_{s1} \to 1$. However, at higher sizes, the absence of N_{u1} and N_{d1} from the definition allows β to converge to high performance quickly and realistically. $\mathcal{C}_{\text{cum}}$ suffers from a converse problem. At s_1 it correctly indicates a zero performance of the filter, but as $s \to s_{\max}$, it converges too slowly onto high efficiency values because it is dragged downwards by the large values of N_{u1} and N_{d1}. We therefore propose a new measure called "alpha efficiency" (so called because it is more fundamental than the beta efficiency), which combines these two parameters in a simple algebraic relationship with the correct asymptotic behavior:

$$\alpha^2 = E^{1/2}\mathcal{C}_{\text{cum}}^{1/2}\left[1 - \{(1-E)(1-\mathcal{C}_{\text{cum}})\}^{1/2}\right] \qquad (11)$$

The alpha efficiency α' is based on the specified particle size as well as those above it, and hence is defined by a similar relationship involving E' rather than E.

The final problem is that β is actually a dynamically changing characteristic of the filter. It is a function of the pass test time t, relative pressure drop $\Delta\mathcal{P}_{\text{rel}}$ and blockage B. t is dependent on flow rate and particle concentration, whereas both $\Delta\mathcal{P}_{\text{rel}}$ and B depend only on the flux of particles challenging the filter, so have one fewer degrees of variability. $\Delta\mathcal{P}_{\text{rel}}$ is a standard parameter in filter testing, so the various measures of efficiency can be usefully compared by expressing them as three-dimensional functions of both s and $\Delta\mathcal{P}_{\text{rel}}$.

For a particular particle size distribution, the performance of the filter also varies according to the order in which the particles hit it. If large particles, particularly in the cake-forming s_4 range, hit first, the filter will block more quickly and some become more efficient for particles of all sizes. Furthermore, C, $\mathcal{C}$, B, E, and α all vary with particle size distribution, for both experimental and simulated filters. Such variability proved a major problem in our study. To control it, we chose to use a distribution of 151 particles numerically proportional to the experimental distribution measured by the particle counter, shown as Default in Figure 2. Other distributions comprised the default distribution with sizes multiplied by 2 (Mult2) or divided by 2, 4, or 8 (Div2, Div4, and Div8, respectively), Figure 2. The sizes of the fines in these distributions were multiplied identically to all the other particles, which could be considered unrealistic, but removed the need for defining the degree of overlap of fines with the other sizes, a problem mentioned earlier. Also, the behavior of the S41 filter was simulated with 3020 particles corresponding to the number of particles (rather than the sizes) of the default distribution multiplied by 20 (Mult#20), and also simulated with this Mult#20 distribution with a single extra particle of size 55 μm.

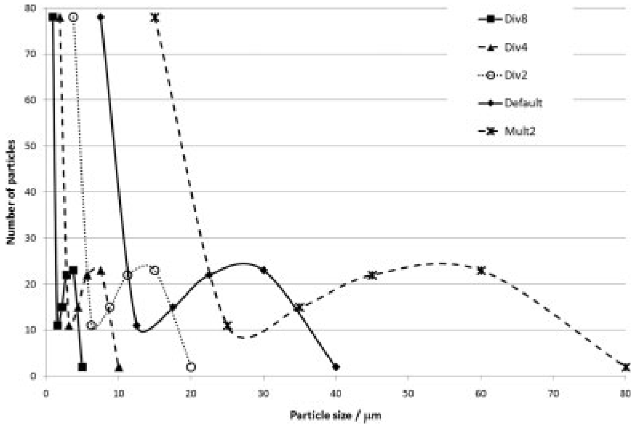

Figure 2. Particle size distributions.

The Model

The filtration model used an existing three-dimensional void network, "Pore-Cor," which has been previously used to model a range of materials such as soil,[21] sandstone[22] and paper coating,[23,24] and range of properties including diffusion.[25] The model approximates the geometry of each void network as a unit cell with periodic boundary conditions, containing 1000 cubic pores connected by up to 3000 cylindrical throats arranged in a regularly spaced Cartesian array. To simulate mercury intrusion, mercury was applied to the maximum z (top) face of the unit cell only, and percolated in the $-z$ direction, i.e., from the top surface downwards in Figure 3. The geometry of the network was adjusted by an eight-dimensional Boltzmann-annealed amoeboid simplex[26,27] to give a close fit to the entire experimental mercury intrusion curve. A simplex is a geometrically defined body which changes its shape and moves around in parameter space searching for the minimum distance between simulation and experiment. Five of the dimensions of the parameter space were defined by continuously variable parameters, namely throat skew, throat spread, pore skew, connectivity, and correlation level. Throat spread (the "fatness" of the throat size distribution) and throat skew (the asymmetry of the distribution) are new variables, described below. If pore skew = 1, then all pores are equal to the size of the biggest throat entering them. In practice, the pores need to be bulked up to match the experimental porosity, by a factor equal to the pore skew. The size distribution of the enlarged pores is

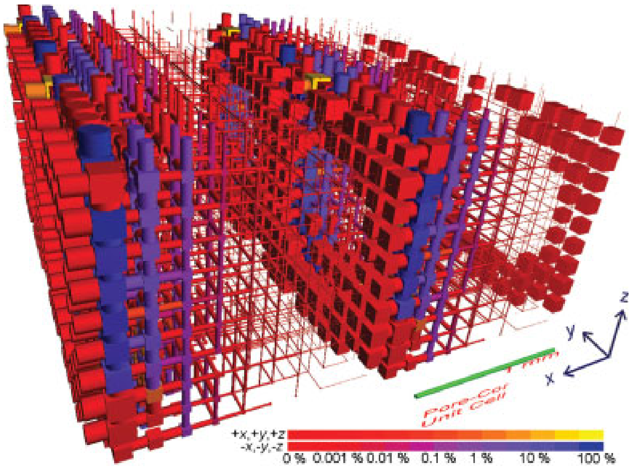

Figure 3. Flow mapping of a vertically banded structure with correlation level 0.95.

[Color figure can be viewed in the online issue, which is available at www.interscience.wiley.com.]

truncated at the previous maximum feature size, with all pores larger than this added to the highest size bin. Connectivity is the average number of throats per pore, ranging from 0 to 6. A typical value when modeling natural samples is 3.5, as in Figure 3. The correlation level κ can vary between 0, for a random structure, and 1 in which throats, and hence adjoining pores, are grouped into pre-determined loci according to their size. In Figure 3, the structure has $\kappa = 0.95$ with respect to loci which are aligned in the *yz* planes with slight curvature towards the respective centers of the four joined unit cells shown in the figure.

There are three additional Boolean dimensions, which, when false, erect a hard, high wall in parameter space. The three Boolean conditions are (i) the network unfragmented, (ii) do all its features separate geometrically without overlap, and (iii) it can achieve the experimental porosity by changing the spacing between rows of features and hence the lengths of the throats.

The new throat size distribution is of a flexible log/Euler-Beta form, which encompasses Gaussian-like, Poisson-like, and bimodal distributions. The probability density function, representing the probability that the distribution lies in a small interval [*x*, *x*+*dx*] is

$$f(x:\zeta,\eta) = \frac{1}{\Psi(\zeta,\eta)} x^{\zeta-1}(1-x)^{\eta-1} \tag{12}$$

where

$$\Psi(\zeta,\eta) = \int_0^1 x^{\zeta-1}(1-x)^{\eta-1}dx \tag{13}$$

is the Euler beta function.

It can be shown that:

$$\zeta = \frac{\mu^2-\mu^3-\mu\sigma^2}{\sigma^2} \tag{14}$$

$$\eta = \frac{\mu-2\mu^2+\mu^3-\sigma^2+\mu\sigma^2}{\sigma^2} \tag{15}$$

The distribution is therefore completely specified if the mean μ and standard deviation σ of the distribution are known.

Throat spread is defined as twice the standard deviation σ. Throat skew has a more complex definition to allow a balanced sampling of the simplex parameter space. It requires four quantities. The first two are the minimum $\mu_{\min}$ and maximum $\mu_{\max}$ means for a given standard deviation:

$$\mu_{\min} = \frac{1}{2}\left(1-\sqrt{1-4\sigma^2}\right) \tag{16}$$

$$\mu_{\max} = \frac{1}{2}\left(1+\sqrt{1-4\sigma^2}\right) \tag{17}$$

These can be found by substituting the following conditions into (14) and (15):

$$\zeta = \eta = 0. \tag{18}$$

If there exists a region where the distribution is unimodal for a given standard deviation then we define the minimum and maximum unimodal means as μ_1 and μ_2, respectively. The boundary case is a uniform distribution with $\zeta = \eta = 1$. μ_1 and μ_2 are obtained by solving a cubic equation, and then choosing the correct root (i.e., the one nearest the median, which is always 0.5)[28]:

$$\mu^3-\mu^2+\mu\sigma^2+\sigma^2 = 0. \tag{19}$$

Percolation

The percolation of mercury is simulated by successive piston-flow intrusion of throats as governed by the Laplace equation:

$$d = \frac{4\gamma\cos\theta}{P_{\mathrm{Hg}}}. \tag{20}$$

The expression gives the diameter *d* of the smallest cylindrical throat in an incompressible solid exposed to mercury, which is intruded when a pressure P_{Hg} is applied to the mercury. γ is the interfacial tension between mercury and air (assumed 0.48 N/m), and θ is the contact angle between the edge of the advancing convex mercury meniscus and the solid surface, assumed to be 140°. These values are typical of those used for mercury intrusion experiments where the true or effective contact angle is unknown. Uncertainties in their values, and the shortcomings of the equation, are well known and have been discussed by van Brakel et al.[29] For most networks with randomly distributed throats following unimodal size distributions, a graph of the Laplace equation size vs. volume intruded gives an s-shaped curve. When P_{Hg} is just large enough for features of size d_c to be intruded, the mercury breaks through from one side of the sample to the other. The point of inflection of the s-shaped curve is usually close to the critical diameter d_c.

The Laplace equation is also used to interpret porometry data. The "Porofil" liquid is designed to be fully wetting, so that $\theta = 0$ and $\cos\theta = 1$. γ is estimated to be 0.016 N/m.

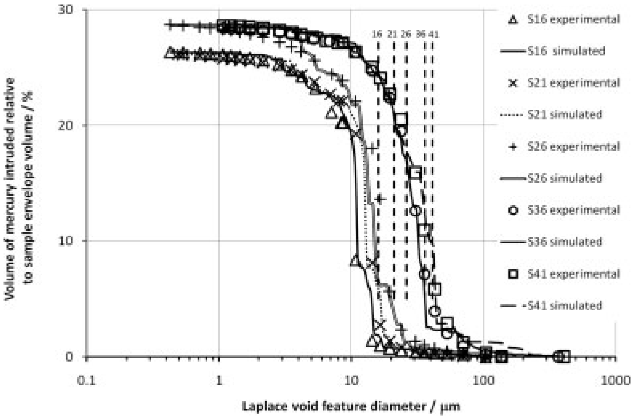

Figure 4. Comparison of experimental and simulated mercury intrusion.

Whereas mercury intrudes before it breaks through the sample, a flow rate in porometry is only detected once breakthrough takes place. Therefore, the breakthrough point is assumed equal to d_c, ignoring any dynamic effects.

Model permeability and flow characteristics

The absolute permeability and flow regime of the simulated structure is found by first calculating the flow capacity F_{arc} of each pore-throat-pore arc within the unit cell network, using parameterized Navier-Stokes equations[30]:

$$F_{\mathrm{arc}} = -\frac{8}{\pi} \cdot \left[\frac{1}{\frac{57}{4L_1^3\left(1+\frac{8.8\lambda}{L_1}\right)} + \frac{8h}{\pi r^4\left(1+\frac{4.4\lambda}{r}\right)} + \frac{57}{4L_2^3\left(1+\frac{8.8\lambda}{L_2}\right)}} \right]. \tag{21}$$

Here h is the length of a throat of radius r connecting two cubic pores with sides L_1 and L_2, respectively. λ is the mean free path between collisions in the fluid. In this case the fluid is hydraulic oil, and λ is taken to be zero. Although λ is pressure and temperature dependant, the slip flow which it predicts changes the flow in a 1 μm tube by only about 1%, so this order-of-magnitude value suffices and does not need to be corrected for temperature or pressure when used to simulate laboratory measurements of absolute permeability. A form of Eq. 21 may also be derived for anisotropic structures in which throats with ellipsoidal or slit-shaped cross-sections join orthorhombic pores.[23]

It is assumed that the flow of liquid through the network is laminar, and so obeys Poiseuille's equation. Combining Poiseuille's equation with the Darcy equation results in an expression for the Darcy permeability independent of the pressure gradient imposed on the sample[23]:

$$k_{\mathrm{sim}} = \frac{\pi}{8} \underset{\mathrm{cell}}{\Omega} (F_{\mathrm{arcs}}) \frac{l_{\mathrm{cell}}}{A_{\mathrm{cell}}}. \tag{22}$$

Here l_{cell} is the length of the unit cell of the network model, and A_{cell} is the cell's cross-sectional area. A network analysis approach to this problem supplies the term $\underset{\mathrm{cell}}{\Omega}(F_{\mathrm{arcs}})$ as the maximal flow capacity through the network of pores and throats. It is calculated by means of the archetypal network capacity algorithm developed by Dinic.[18] There is an overall conservation of flow, so that the entire volume of fluid entering the top of the unit cell emerges at the bottom, with no build-up through the network. The value obtained, as the maximal flow, is based on the capacities of only the channels found to carry flow. The solution derived is analogous to the "trickle flow" of an incompressible fluid, which finds various tracks through the unit cell in the $\pm x$, $\pm y$, and $-z$, directions, Figure 3. Flow along each trickle-flow route is limited by the arc along the route with least flow capacity, so the overall flow solution is closely related to d_c. The present solution converges on the full solution to multiple simultaneous Navier-Stokes equations for unit cells with straightforward flow paths, which are more likely to occur through networks of void features which have simple connectivity and cover a small size range. In practice, however, full solutions to the Navier-Stokes equations always require pruning of the relevant matrices, and the current method can be regarded as analogous to an automatically pruned Navier-Stokes solution. As will be seen, the trickle flow and pruning approximations cause an underestimate of the absolute permeability, but allow trends between similar samples to be simulated and predicted. The current method is a more precise approximation than the other main methods of solving the flow in void networks, namely the resistor network[7] and effective medium approximations.[31,32]

The effective net flow of a given arc from a given node was elucidated and represented visually along each of the individual directions (positive and negative directions) on each Cartesian axis. The net flows are shown with red (light gray) to blue (dark gray) color gradation in the positive Cartesian directions and in a red (light gray) to yellow (lightest gray) color gradient in the negative Cartesian direction, Figure 3.

The permeabilities k of the simulated filters were used for the calculation of their pressure drops by re-arranging the Darcy equation as shown:

Table 2. Minimum and Maximum Feature Diameters, Fitting Parameters, and Distance (Goodness of Fit) for the First Stochastic Realisation for Each Filter

Sample	Minimum Feature Diameter (μm)	Maximum Feature Diameter (μm)	Porosity (%)	Throat Skew	Throat Spread	Pore Skew	Connectivity	Correlation Level	Distance
S16	0.428	103.59	26.30	−12.52	0.477	3.646	4.52	0.322	0.94
S21	0.492	122.02	26.13	−12.53	0.477	3.646	4.52	0.322	1.00
S26	0.429	174.99	28.65	−13.85	0.470	3.062	4.44	0.212	1.38
S36	1.080	366.53	28.41	−12.29	0.485	2.909	3.90	0.161	0.86
S41	1.075	403.70	28.58	−0.54	0.500	2.288	3.34	0.292	1.40

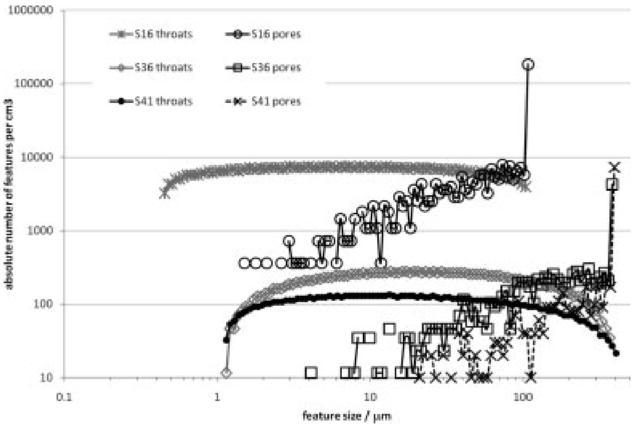

Figure 5. Absolute numbers of pores and throats/cm^3 of sample in the simulations of filters S16, S36, and S41.

$$\delta P_{\text{filter}} = -\frac{\mu\, l_{\text{filter}} \left(\frac{dv}{dt}\right)_{\text{filter}}}{k\, A_{\text{filter}}}. \tag{23}$$

Results

Figure 4 shows the experimental mercury intrusions curves of all the filters, with the pressure converted to intruded size via Eq. 20. The maximum size $d_{\max}$ and minimum size $d_{\min}$ of each curve is used by the model to generate the maximum and minimum void feature sizes in the model. So that these scale correctly between each sample, the lengths of the asymptotes have been scaled relative to the sizes at which intrusion is 90% and 10% of maximum, d_{10} and d_{90}. For all the intrusion curves shown, $d_{10}/d_{\max} = 0.132$, and $d_{90}/d_{\min} = 11.6$. Also, shown are the simulations fitted by the Simplex, which can be seen to match closely overall, and to model most of the subtle differences around the points of inflexion. As mentioned previously, the naming of the filter grades was based on porometry and pass tests, not on porosimetry. Nevertheless, for interest, dashed lines are shown at the named sizes of 16, 21, 26, 36, and 41 μm. For S16, S21, and S26, the sizes can be seen to correlate with the take-off points of the intrusion curves from the bottom (zero intrusion) axis as applied mercury pressure increases and Laplace size, Eq. 20, decreases. For S36 and S41, the named sizes are close to the points of inflection, which are also approximately equal to the breakthrough diameters d_c.

The intrusion curves were corrected for sample compression effects using Pore-Comp software[20] and then fitted with the simplex, as described earlier. The simulated intrusion curves for the first stochastic realization for each filter are shown in Figure 4, and the corresponding parameters in Table 2. Also, shown in Table 2 are the distances between the

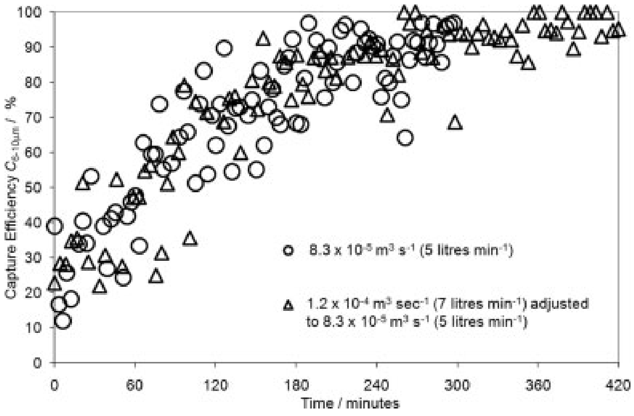

Figure 6. Comparison of capture efficiency *C* over size interval 6–10 μm at flow rates of 8.3 × 10^{-5} m^3/s (5 l/min), and 1.2 × 10^{-4} m^3/s (7 l/min) adjusted back to 8.3 × 10^{-5} m^3/s (5 l/min).

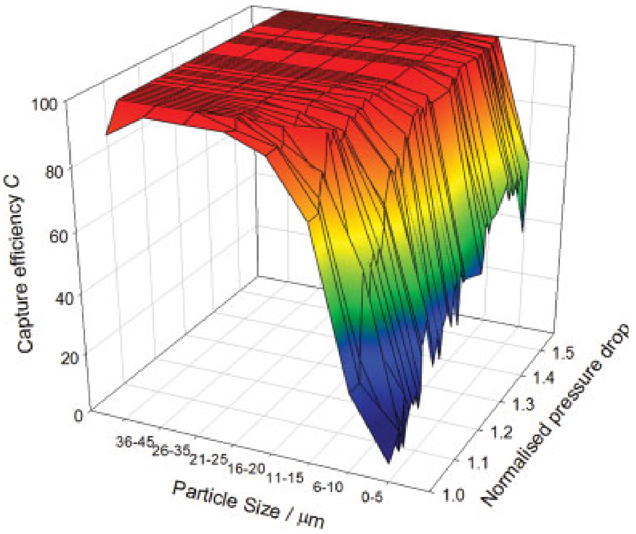

Figure 7. Experimental single-pass efficiency *C* (ΔP_{rel}, *s*) of S36 at a flow rate of 8.3 × 10^{-5} m^3/s (5 l/min).

[Color figure can be viewed in the online issue, which is available at www.interscience.wiley.com.]

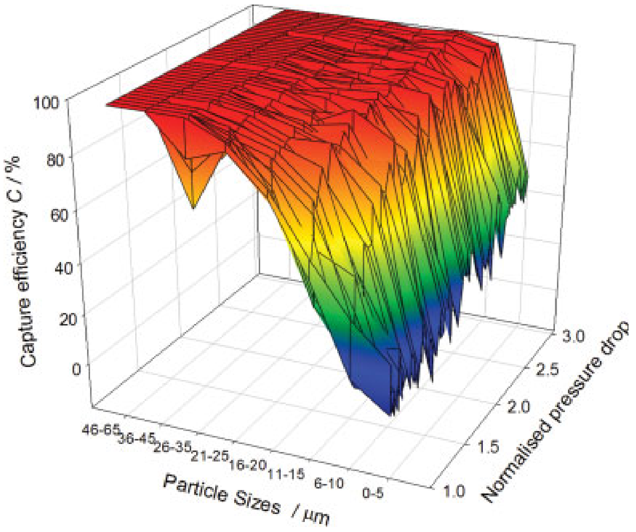

Figure 8. Experimental single-pass efficiency *C* (ΔP_{rel}, *s*) of S41 at a flow rate of 8.3 × 10^{-5} m^3/s (5 l/min).

[Color figure can be viewed in the online issue, which is available at www.interscience.wiley.com.]

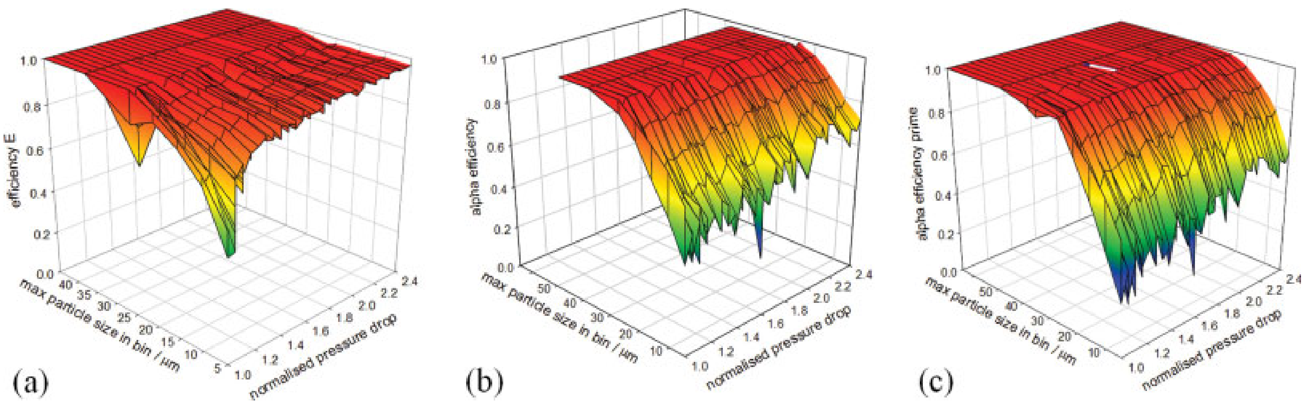

Figure 9. Other experimentally based measures of the efficiency of S41.

(a) $E(\Delta P_{\text{rel}}, s)$, (b) $\alpha(\Delta P_{\text{rel}}, s)$, and (c) $\alpha'(\Delta P_{\text{rel}}, s)$. [Color figure can be viewed in the online issue, which is available at www.interscience.wiley.com.]

experimental and simulated curves shown in Figure 4, using a normalized parameter which tends to zero as the fit becomes perfect. The absolute numbers of pores and throats/cm^3 of the simulations of filters S16, S36, and S41, calculated from Eqs. 12–19, are shown in Figure 5.

Particle capture efficiencies were measured at various flow rates to find a rate at which there were no rate-dependant effects. A flow rate of 5.8×10^{-5} m^3/s (3.5 l/min) proved insufficient to transport all of the contaminant around the rig, leading to fluctuations in the concentration of contaminant challenging the filter. Tests at flow rates of 8.3×10^{-5} m^3/s and 1.2×10^{-4} m^3/s showed a stable upstream contaminant concentration, no filter caking, and capture efficiencies that were independent of rate, Figure 6. All subsequent tests therefore used these latter two flow rates.

The efficiencies C $(\Delta\mathcal{P}_{\text{rel}}, s)$ of filters S36 and S41 measured using the single pass protocol, Figure 1, at 8.3×10^{-5} m^3/s are shown in Figures 7 and 8, respectively. Figures 9a–c show the corresponding efficiency E (Eq. 6), and alpha efficiencies α and α' (Eq. 11) of S41 at 8.3×10^{5} m^3/s. The experimental permeabilities k_{exptl} were measured by finding the flow of water through the filter at a fixed pressure head of 10 cm water gauge or 970 Pa, and are shown in Table 1. In Figure 10 they are compared with the means and standard deviations of the absolute permeabilities k_{sim} of the first 10 stochastic realizations for each filter, calculated from Eqs. 21 and 22. It can be seen that the simulated values are between 0.7 and 1.6 orders of magnitude (powers of ten) too low, and that the simulated values trend more slowly than the experimental values. The linear regression on the log-log plot has a coefficient of determination R^2 of 0.77.

To simulate the filtration process, individual particles were selected from one of the size distributions shown in Figure 2, with the probability of a particle being selected being proportional to the remaining number of particles in its size bin. Each particle was fed through the maximal flow route. If straining occurred, all flow routes were recalculated. Filter characteristics were calculated according to Eqs. 1–11 and 21–23. Figure 11 shows a comparison of the efficiencies of all the filters, measured using the default particle distribution. Examples of the progressive blockage of filters S16, S36, and S41, when challenged with the distributions shown in Figure 2, are shown in Figure 12. The results range from the rapid blockage of S16 by the default distribution (+), to the absence or near absence of blockage of S16 by Div8 (△), S36 by Div2 (◇), and S41 by Div2 (●).

Figures 13 and 14 show the simulations of C $(\Delta\mathcal{P}_{\text{rel}}, s)$ for S36 and S41 plotted over the same ranges as the experimental results in Figures 7 and 8. It can be seen that the

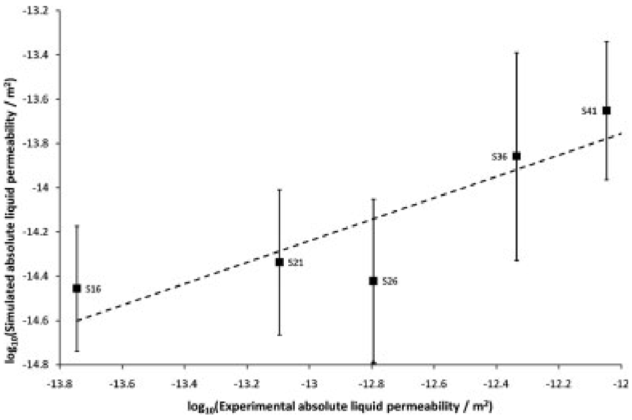

Figure 10. Comparison of experimental and simulated absolute permeabilities.

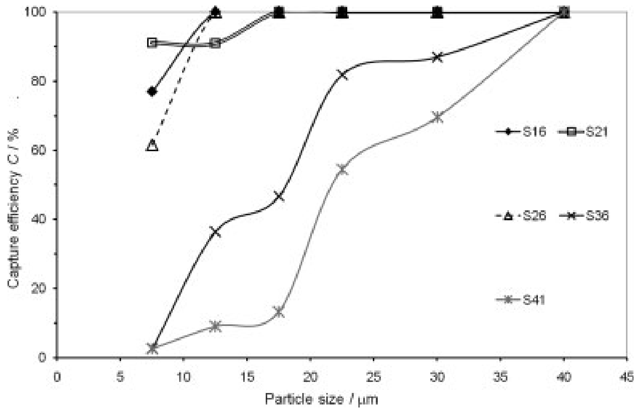

Figure 11. Comparison of the simulated efficiencies of all the filters using the default particle distributions.

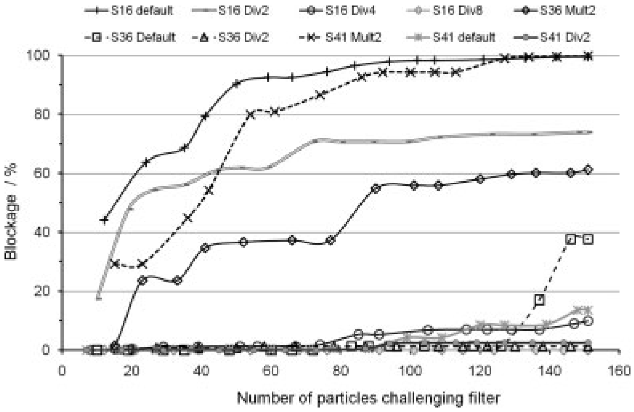

Figure 12. Comparison of the simulated blockage of filters S16, S36, and S41 when challenged by the particle distributions shown in Figure 2.

efficiencies are unstable at low particles numbers (low normalized pressure drop). The efficiency of the S36 stays constant in the simulation, whereas the efficiency of S41 simulation builds up initially and then drops off for $\Delta\mathcal{P}_{\mathrm{rel}} > 2.1$. Even using the 3020 particles of Mult#20, $\Delta\mathcal{P}_{\mathrm{rel}}$ of S41 did not rise above 2.4, and its capture efficiency profile remained constant. However, on mixing one particle of size 55 μm into this distribution, i.e., to an additional number density of only 0.03%, the pressure drop was found to rise substantially, to $\Delta\mathcal{P}_{\mathrm{rel}} = 210$, while the capture efficiency profile continued to remain constant.

Figure 15 shows the complete flow mapping of the S41 simulation for the clean ($\Delta\mathcal{P}_{\mathrm{rel}} = 1$) and 54% blocked filter ($\Delta\mathcal{P}_{\mathrm{rel}} = 2.18$). The features blocked due to straining are shown green in the lower figure, but are too small to see at that magnification. However, they can be viewed in virtual reality, and by close-up inspection of a wire-frame version of the structure. Such examinations show that most straining occurs near the surface (high z) as expected, but that several features are also blocked at much lower z.

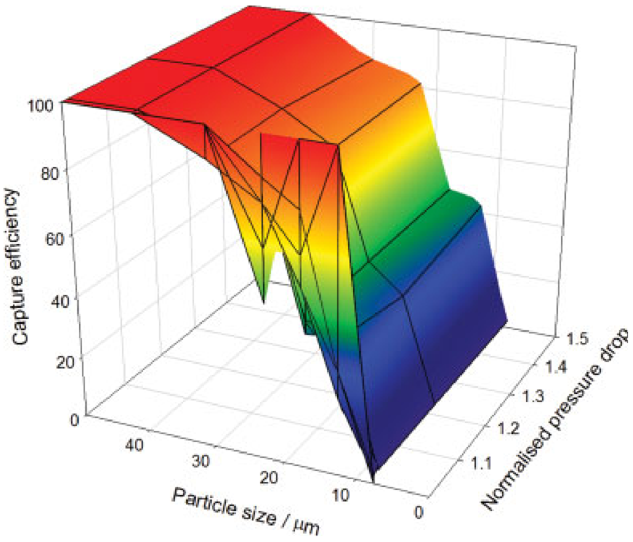

Figure 13. Simulation of S36 after challenge by default distribution, for direct comparison with Figure 7.

[Color figure can be viewed in the online issue, which is available at www.interscience.wiley.com.]

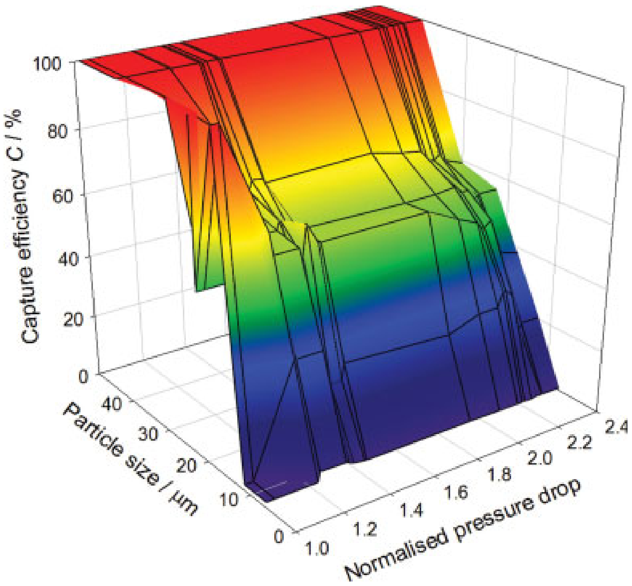

Figure 14. Simulation of S41 after challenge by three lots of the default distribution, for comparison with Figure 8.

[Color figure can be viewed in the online issue, which is available at www.interscience.wiley.com.]

Discussion

Figure 10 shows that although the network model simulates the correct qualitative trend, it underestimates the absolute permeabilities of the filter by around 1 order of magnitude, and trends too slowly across the series of samples. The stochastic scatters of the realizations, expressed in terms of standard deviations, are also high. The model has previously exhibited similar characteristics in the prediction of the absolute permeabilities of sandstones.[22] The discrepancies arise because of the approximations inherent in the network and calculation methods described earlier. However, such simplifications are essential to make the filtration simulations computable on fast personal computers rather than supercomputers, an essential requirement for a model useful to industry.

Comparison of Figures 13 and 14 with Figures 7 and 8 shows that the simulations tend to underestimate the capture efficiencies C in the middle of the particle size range. The build up of C with $\Delta\mathcal{P}_{\mathrm{rel}}$ evident in Figures 7 and 8 is largely masked in the simulations by the inevitable instability in the results at very low particle number and hence low $\Delta\mathcal{P}_{\mathrm{rel}}$. However, since the simulation is essentially *a priori*, the level of agreement is encouraging, and sufficiently close to offer an alternative to single pass testing. It is also useful for this purpose that the simulations are relatively stable with respect to slight changes in the particle size distributions, even though the simulated pressure drop is not. The sensitivity of the pressure drop to very small additions of large particles opens the possibility of simulating pre-filters.

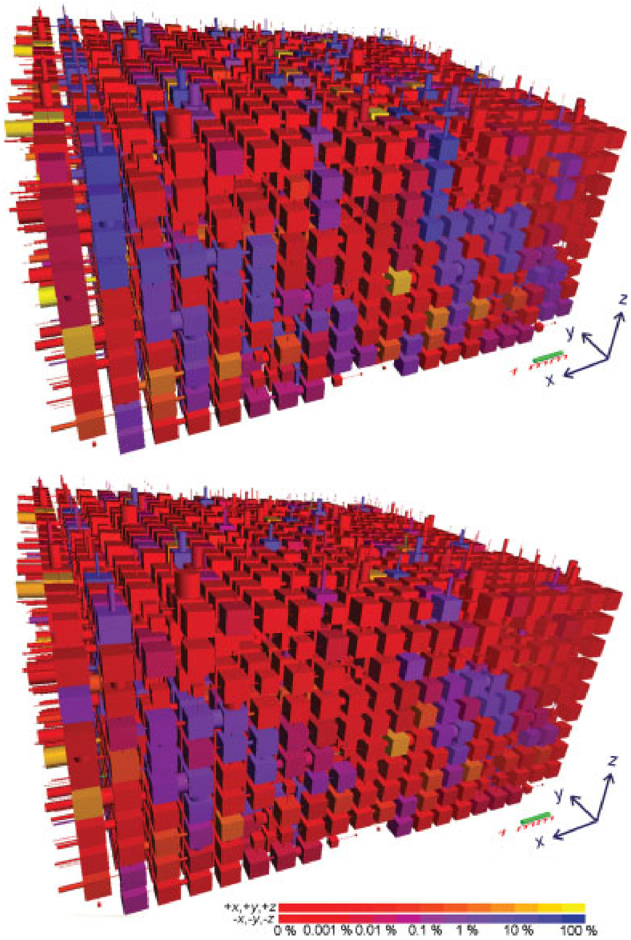

Figure 15. Flow paths of filter S41 when clean (top), and after challenge by three lots of the default distribution shown in Figure 2, causing a blockage B of 54% (ΔP_{rel} = 2.18).

[Color figure can be viewed in the online issue, which is available at www.interscience.wiley.com.]

Inspection of Figures 9a, b reveals that the neither the efficiency E nor the alpha efficiency α are good measures of overall filter performance as judged from the capture efficiencies. However, α' (ΔP_{rel}, s), Figure 9c, performs the required role of providing an averaged and summed measure of the filter performance, which as can be seen has the correct asymptotic behavior. The beta efficiency is generally an ill-behaved measure to use, because it tends to infinity as the filtration efficiency increases, so is difficult to handle mathematically.

Conclusions and Future Work

An important feature of the simulations is that after fitting to the percolation characteristic of the material, as measured in this case by the mercury porosimetry, they require no arbitrary calibration or training sets. Therefore, any filter for which mercury intrusion or void geometric data is available can be simulated.

The simulations do not yet take account of filtration by particle deposition other than straining, and concertive effects of particles forming aggregates. If an experimental filter is exposed to fines only, it will eventually clog because of these effects, whereas at present the simulation will never clog. The lack of concertive effects also explains the underestimates of filter efficiency in the middle of the particle size ranges. Furthermore, because of the small number of particles in the simulation, the results have to be based on cumulative averages over the whole history of the simulation. Thus, initial low efficiencies can drag down the efficiencies at higher pressure drop. This does not occur in the experimental curves, which are based on independent measurements at each pressure drop. For example the dip in efficiency at 26–35 μm at a pressure drop of 1.17, Figure 8, is not reflected in adjacent independent measurements.

The lack of arbitrary fitting parameters allows greater confidence in the simulation of other effects. For example, the ageing of filters can be observed by increasing the numbers of particles challenging the filters. Also, some simulations show that the capture efficiency builds up initially, but then ceases to increase because of channeling of the flow routes.

Future simulations will include deposition processes other than straining. Also, a method has been developed to base the filtration simulation on porometry rather than porosimetry data, thus avoiding the contentious use of mercury.

Literature Cited

1. Purchas DB. A practical view of filtration theory. *Filtration*. 2004; 75–81.
2. Herzig JP, Leclerc DM, LeGoff P. Flow of suspensions through porous media—application to deep-bed filtration. *Ind Eng Chem*. 1970;62:9–35.
3. Redner S, Datta S. Clogging time of a filter. *Phys Rev Lett*. 2000; 84:6018–6021.
4. Dickenson TC. *Filters and Filtration Handbook*, 4th ed. Oxford, UK: Elsevier Advanced Technology, 1997.
5. Fatt I. The network model of porous media III. Dynamic properties of networks with tube radius distribution. *Pet Trans AIME*. 1956; 207:164–177.
6. Lee J, Koplik J. Network model for deep bed filtration. *Phys Fluids*. 2001;13:1076–1086.
7. Martins AA, Laranjeira PE, Lopes JCB, Dias MM. Network modeling of flow in a packed bed. *AIChE J*. 2007;53:91–107.
8. Dullien FAL, Batra VK. Determination of the structure of porous media. *Ind Eng Chem Res*. 1970;62:25–53.
9. Rege SD, Fogler HS. A network model for deep bed filtration of solid particles and emulsion drops. *AIChE J*. 1988;34:1761–1772.
10. Imdakm AO, Sahimi M. Computer-simulation of particle-transport processes in flow through porous-media. *Chem Eng Sci*. 1991;46: 1977–1993.
11. Sahimi M, Imdakm AO. Hydrodynamics of particulate motion in porous-media. *Phys Rev Lett*. 1991;66:1169–1172.
12. Imdakm AO, Sahimi M. Transport of large particles in flow through porous-media. *Phys Rev A*. 1987;36:5304–5309.
13. Osmak S, Gosak D, Glasnovic A. Dynamic mathematical model of deep bed filtration process. *Comput Chem Eng*. 1997;21:S763–S768.
14. Sahimi M, Gavalas GR, Tsotsis TT. Statistical and continuum models of fluid solid reactions in porous-media. *Chem Eng Sci*. 1990; 45:1443–1502.
15. Elmelech M, Xiadong J, Gregory J, Williams R. *Particle Deposition and Aggregation: Measurement, Modelling and Simulation*. Butterworth-Heinemann, Elsevier, 1998.
16. Sexton J. *Modelling Filter Media to Determine Filtration Efficiency, Characterisation, Filter Testing and Quality Standards*. Runcorn, 2003.

17. Constantinides GN, Payatakes AC. A 3 dimensional network model for consolidated porous-media—basic studies. *Chem Eng Commun*. 1989;81:55–81.
18. Ahuja RK, Kodialam M, Mishra AK, Orlin JB. Computational investigations of maximum flow algorithms. *Eur J Oper Res*. 1997;97:509–542.
19. Matthews GP, Moss AK, Ridgway CJ. The effects of correlated networks on mercury intrusion simulations and permeabilities of sandstone and other porous media. *Powder Technol*. 1995;83:61–77.
20. Gane PAC, Kettle JP, Matthews GP, Ridgway CJ. Void space structure of compressible polymer spheres and consolidated calcium carbonate paper-coating formulations. *Ind Eng Chem Res*. 1995;35: 1753–1764.
21. Holtham DAL, Matthews GP, Scholefield DS. Measurement and simulation of the void structure and hydraulic changes caused by root-induced soil structuring under white clover compared to ryegrass. *Geoderma*. 2007;142:142–151.
22. Matthews GP, Canonville C, Moss AK. Use of a void network model to correlate porosity, mercury porosimetry, thin section, absolute permeability and NMR relaxation time data for sandstone rocks. *Phys Rev E*. 2006;73:031307.
23. Bodurtha P, Matthews GP, Kettle JP, Roy IM. Influence of anisotropy on the dynamic wetting and permeation of paper coatings. *J Colloid Interface Sci*. 2005;283:171–189.
24. Laudone GM, Matthews GP, Gane PA, Ridgway CJ, Schoelkopf J. Estimation of the effective particle sizes within a paper coating layer using a void network model. *Chem Eng Sci*. 2005;60:6795–6802.
25. Laudone GM, Matthews GP, Gane PAC. Modelling diffusion from simulated porous structures. *Chem Eng Sci*. 2008;63:1987–1996.
26. Johnson A, Roy IM, Matthews GP, Patel D. An improved simulation of void structure, water retention and hydraulic conductivity in soil, using the pore-cor three-dimensional network. *Eur J Soil Sci*. 2003;54:477–489.
27. Press WH, Teukolsky SA. Simulated annealing optimization over continuous spaces. *Comput Phys*. 1991;5:426–429.
28. Press WH, Flannery BP, Teukolsky SA, Vetterling WT. Evaluation of functions. In: idem. *Numerical Recipes: The Art of Scientific Computing*, 1st ed. Cambridge: Cambridge University Press, 1986:145–146.
29. van Brakel J, Modry S, Svata M. Mercury porosimetry: state of the art. *Powder Technol*. 1981;29:1–12.
30. Scheidegger AE. *The Physics of Flow Through Porous Media*. Toronto: University of Toronto Press, 1974.
31. Stamatakis K, Tien C. Dynamics of batch sedimentation of polydispersed suspensions. *Powder Technol*. 1988;56:105–117.
32. Berg CR. A simple, effective medium model for water saturation in porous rocks. *Geophysics*. 1995;60:1070–1080.

Manuscript received Jul. 30, 2008, and revision received Feb. 23, 2009.